JPL Document D-92350

TECHNOLOGY DEVELOPMENT FOR EXOPLANET MISSONS

Technology Milestone #1 Report:
Vortex Coronagraph Technology

Gene Serabyn, P.I.
John Trauger, Dwight Moody, Dimitri Mawet,
John Krist and Brian Kern

23 May 2014

Approvals:

Released by

[signature]

Gene Serabyn

Principal Investigator

5/27/2014

Date

Approved by

[signature]

Peter Lawson

Exoplanet Exploration Program Chief Technologist, JPL

5/28/2014

Date

[signature]

Nick Siegler

Exoplanet Exploration Program Technology Manager, JPL

5/28/14

Date

[signature]

Gary Blackwood

Exoplanet Exploration Program Manager, JPL

6/2/2014

Date

[signature]

Douglas Hudgins

Exoplanet Exploration Program Scientist, NASA HQ

6/23/14

Date

[signature]

John Gagosian

Exoplanet Exploration Program Executive, NASA HQ

6/23/14

Date

1

Table of Contents

TDEM Milestone #1 Report:
Vortex Coronagraph Technology

1. Overview

We report the results of our ROSES Technology Development for Exoplanet Missions (TDEM) research in pursuit of ***Demonstrations of Deep Starlight Rejection with a Vortex Coronagraph***. Our March 2012 homonymous White Paper specified the milestone objective, success criteria, and methodology for computing the milestone metrics. This report follows the general outline of that White Paper, but includes the specifications for the specific vortex mask that was used to achieve the milestone level, the optical configuration employed in JPL's High Contrast Imaging Testbed (HCIT), the experimental approach, the final measurements, and the analysis of the results. Our main accomplishment has been to surpass the targeted monochromatic performance milestone, on three separate occasions. The first high contrast monochromatic milestone for the vortex coronagraph has thus been met.

2. Description of the Technology Milestone

TDEM Technology Milestones are intended to document progress in the development of key technologies for potential space-based missions that would detect and characterize exoplanets, such as a facility-class TPF-C (Levine et al. 2006), a probe-scale ACCESS (Trauger et al. 2010) or Exo-C mission, or a smaller Explorer-class mission.

This milestone addresses monochromatic starlight suppression with the vortex coronagraph. The objective of this TDEM milestone is the validation of a vortex focal plane mask with monochromatic light. This milestone thus focuses on the validation of one key TDEM technology – the vortex mask. Success is defined in terms of statistically significant performance demonstrations of this key technology, ideally with minimal sensitivity or dependence on extraneous environmental factors. The milestone is:

Vortex Milestone 1 definition:
Narrowband Starlight Suppression with Vortex Masks

Using vortex masks, demonstrate a calibrated coronagraph contrast of 1×10^{-9} at angular separations of 3 λ/D to 8 λ/D, at a wavelength, λ, in the range 400 –900 nm, for at least one polarization state.

The "angular separations" are defined in terms of the wavelength, λ, and the diameter, D, of the aperture stop on the deformable mirror (DM), which is the pupil-defining element of the laboratory coronagraph. For this milestone, vortex masks will be used in an approximately f/50 to f/100 beam, corresponding to the current HCIT configuration with a pupil stop at the deformable mirror (DM) of at least 16 mm diameter.

The specific DM used in our HCIT experiments has 1024 actuators controlling the surface of a 48×48 mm mirror facesheet, which is masked by the aforementioned pupil stop. The minimum pupil diameter of 16 mm was originally specified to allow for the

potential use of off-the-shelf polarization components, some of which could have vignetted the beam at a diameter of somewhat under an inch. However, by installing our polarization optics in the smaller beam diameter region prior to the source pinhole (cf. Sect. 2.4), for which a new mounting and removal arrangement was developed, this previously foreseen upper limitation to the pupil diameter was eliminated. The final DM aperture stop of 24 mm that was employed for the three milestone runs thus exceeded 16 mm significantly. For this 24 mm stop, the beam focal ratio at the vortex mask was 64.3.

2.1. Relevance for a Future Exoplanet Mission

Development of vortex technology is intended to advance the readiness of a mission concept for the coronagraphic imaging and spectroscopic observation of exoplanetary systems. The small inner working angle (IWA) capability of the vortex coronagraph allows consideration of a range of mission sizes, from several-meter diameter flagship missions to much smaller Explorer-class missions.

To detect exoplanets in the super-Earth to Jovian range, a coronagraph must provide raw image contrast of $\approx 10^{-9}$ in a dark field between an IWA and an outer working angle (OWA) near the parent star. It is expected that post-processing of coronagraph data will provide detection sensitivities to planets and debris disks an order of magnitude fainter (Trauger and Traub 2007). Therefore, this milestone requires a demonstration of a high contrast dark field at the 10^{-9} level.

Exoplanet imaging missions form a high contrast "dark field" over working angles spanning $n_i\lambda/D$ to $n_o\lambda/2D$, where $n_i\lambda/D$ corresponds to the IWA, as defined by the science requirements and as specified in the wavefront control algorithm, and $n_o\lambda/D$ corresponds to the OWA of the targeted dark hole, i.e., the radius out to which the wave front control algorithm is chosen to be applied. The TPF-C science requirements were an IWA of $4\lambda/D$ (Levine et al. 2006), but as smaller values are possible with the vortex coronagraph, we selected $3\lambda/D$ for our IWA in this milestone, significantly smaller than the TPF-C requirement. The OWA was set to be $8\lambda/D$, as specified in our vortex milestone white paper. This OWA specification was originally chosen because earlier demonstrations and extensive optical modeling and tolerancing had shown that it is increasingly difficult to control the dark field contrast as one moves closer to the image of the target star, meaning that a larger OWA can be used to lower the *average* contrast in the dark hole simply by annexing even darker more distant regions. However, as our aim was low contrasts in the most challenging inner region of the image plane, use of a larger OWA would have been counterproductive. **We thus emphasize that there was in fact no impediment at all to using a larger OWA; rather, the OWA was specified at 8 λ/D solely to exclude even darker outer regions and thus to make it *more difficult* to achieve the milestone.** Our OWA of $8\lambda/D$ is thus not a limitation in any real sense at all.

Finally, for completeness, we note that a 24 mm DM aperture stop could have been used to provide an OWA of up to almost $12\lambda/D$, because in principle, $n_o \leq n_{DM}/2$, where n_{DM} is the number of actuators across the exposed aperture of the DM (and $n_{DM} = 24$ here). To generate a dark hole with a smaller OWA than this maximum, the wavefront control algorithm applied to the DM was thus simply specified to control only spatial frequencies up to $n_o\lambda/D$, with $n_o = 8$, rather than the maximum possible frequency of $12\lambda/D$.

The contrast specification relates to the average contrast level in the dark field of interest around the source or parent star, the same criterion used in earlier HCIT milestones for other coronagraphs. It should be applicable to any coronagraph that propagates its image from sky to the coronagraph focal plane without optical distortions. Analysis of contrast in the dark field (if close to the target value) must necessarily account for the statistical nature of the static and "quasi-static" speckle patterns. The milestone measurements themselves will result in a distribution of speckle intensities, from which one can estimate the average contrast and statistical confidence levels. Statistical measures of both the average intensity and its variance in the coronagraph dark field are provided in support of the milestone validation package, as specified in Section 5 below. However, as stated in the milestone specification white paper, if the result is well below the milestone target, the statistical analysis can be minimal.

2.2. The Vortex Coronagraph

Among the four major coronagraph types, the optical vortex coronagraph brings the advantages of a small inner working angle, high transmission, a clear off-axis field of view, and compatibility with the layout of the Lyot coronagraph (Guyon et al. 2006; Mawet et al. 2009; Serabyn et al. 2010).

The operation of an ideal optical vortex coronagraph is as follows (Mawet et al. 2005; Swartzlander 2009, Serabyn & Mawet 2012a). A clear telescope input pupil can be described by a field distribution, $P_i(r)$, of

$$P_i(r) = \begin{cases} 1 & \text{for} \quad r < A \\ 0 & \text{for} \quad r > A, \end{cases} \tag{1}$$

where r is the radial coordinate, and A is the radius of the input aperture. Focusing the light leads, via a Fourier transform, to the usual focal-plane field distribution,

$$E_f(\theta) \propto \frac{J_1(kA\theta)}{kA\theta}, \tag{2}$$

where J_1 is the Bessel function of order 1, k is the wavenumber, and θ is the angular radial offset from the center of the stellar PSF.

Centering a transmissive vortex phase mask on this focal plane point spread function multiplies the ideal focal plane field distribution by a phase factor corresponding to an azimuthal phase ramp, i.e., $e^{in\alpha}$, where α is the azimuthal angle, and n is the "topological charge" of the vortex (i.e., the number of 2π's of phase the mask provides for one circuit about the center), yielding

$$E_f(\theta, \alpha) \propto e^{in\alpha} \frac{J_1(kA\theta)}{kA\theta}. \tag{3}$$

After passage through the focal plane vortex phase mask, the light is recollimated, and an image of the pupil is formed. This pupil arises by the usual Fourier transform relationship between focal and pupil planes, and because of the extra phase factor, and the properties of Bessel functions, specifically

$$J_n(x) = \int_{-\pi}^{\pi} e^{-i(n\varphi - x\sin(\varphi))} \, d\varphi, \tag{4}$$

where J_n refers to Bessel functions of order n, the final pupil plane distribution is proportional to (Mawet et al. 2005; Swartzlander 2009; Serabyn & Mawet 2012a)

$$\int_0^{\infty} J_n(kr\theta)J_1(kA\theta)d\theta \tag{5}$$

instead of the usual

$$\int_0^{\infty} J_0(kr\theta)J_1(kA\theta)d\theta. \tag{6}$$

This modest change in the integrand has the effect of changing the resultant pupil distribution dramatically: instead of the original uniformly illuminated pupil (i.e., with all of the light inside the entrance pupil), a distribution with all of the light outside of the original pupil results, i.e., the reimaged region of the interior of the original pupil has uniformly zero intensity. In the post-vortex pupil, the electric field falls off as r^{-2} for a charge 2 vortex (Fig. 1, top right panel), while for higher order vortices, similarly clear pupil interiors ensue, but the external radial profiles include higher powers of r^{-2} as well, leading to multiple rings. In the ideal case, the starlight is then completely blocked by a simple opaque stop in the downstream pupil plane that is matched to the pupil radius. Of course with wavefront aberrations present, residual light will appear inside the pupil.
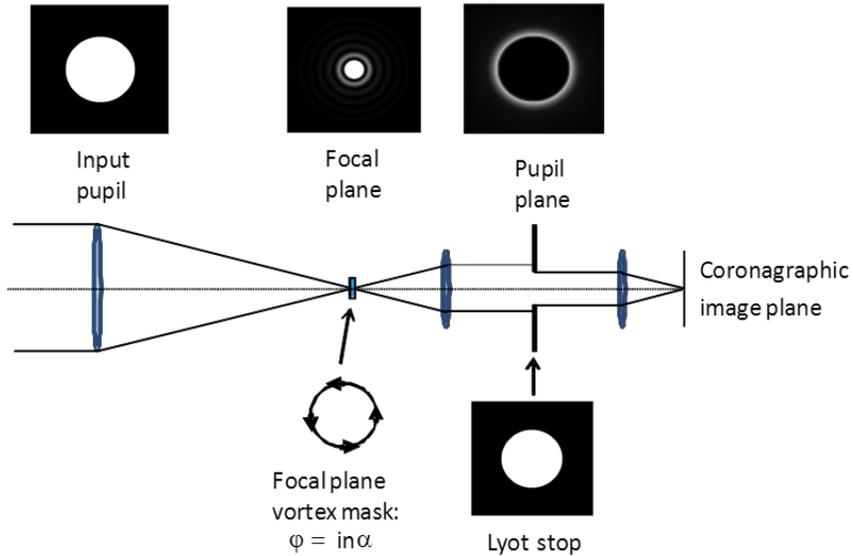

Figure 1. *Layout of the optical vortex coronagraph: an optical vortex phase mask in the focal plane yields a downstream pupil image in which all of the on-axis starlight appears outside of the original pupil's image, where it is blocked by an aperture (Lyot) stop.*

2.3. The Vortex Mask

This TDEM award supported the testing of general vortex masks in the HCIT, and as our baseline plan, we focused on the testing of vector vortex phase masks manufactured out of liquid crystal polymers (LCP). A detailed discussion of the different types of vortex mask and of their relative advantages and disadvantages is provided in Mawet et al. (2011a). The mask used to meet the milestone, manufactured by JDS Uniphase, is seen in Figure 2 through a polarizing microscope and a Mueller matrix imaging polarimeter, and a cross-sectional view of the structure of this mask is shown in Figure 3 (Mawet et al. 2009). The mask used to meet the milestone is the same JDSU mask as used for earlier tests (Mawet et al 2011a,b; Serabyn et al. 2012b); its specifications are given in Table 1.
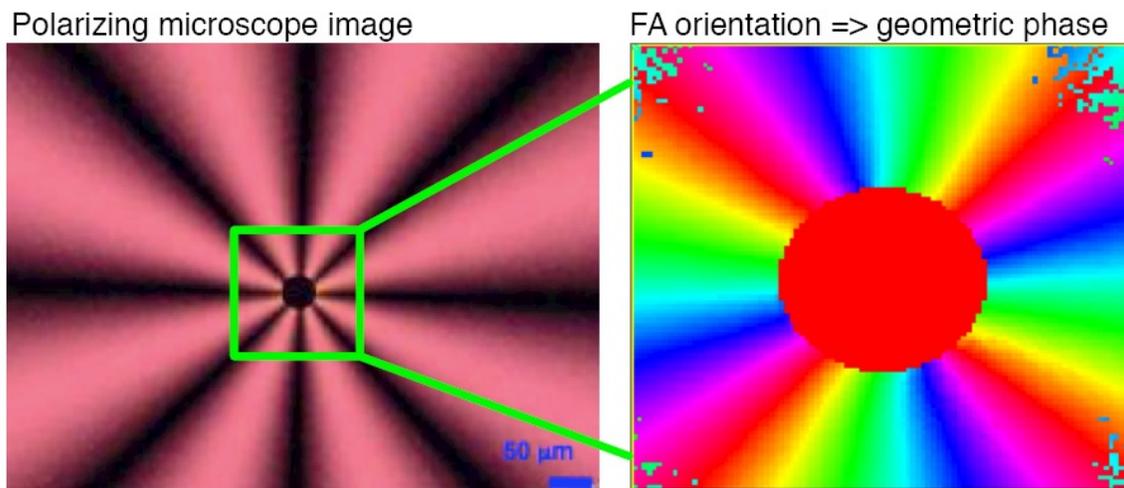
Figure 2. *Left: A fourth-order liquid crystal polymer vortex phase mask between crossed polarizers. Right: zoom on the central part using a polarimetric microscope, as measured at the Univ. of Arizona, showing the fast axis orientation rotating about the center. Here, this rotation yields a geometric phase change equals to 4θ, where θ is the focal plane azimuthal coordinate, subsequently spanning 4 waves or 8π. (Mawet et al. 2011b).*
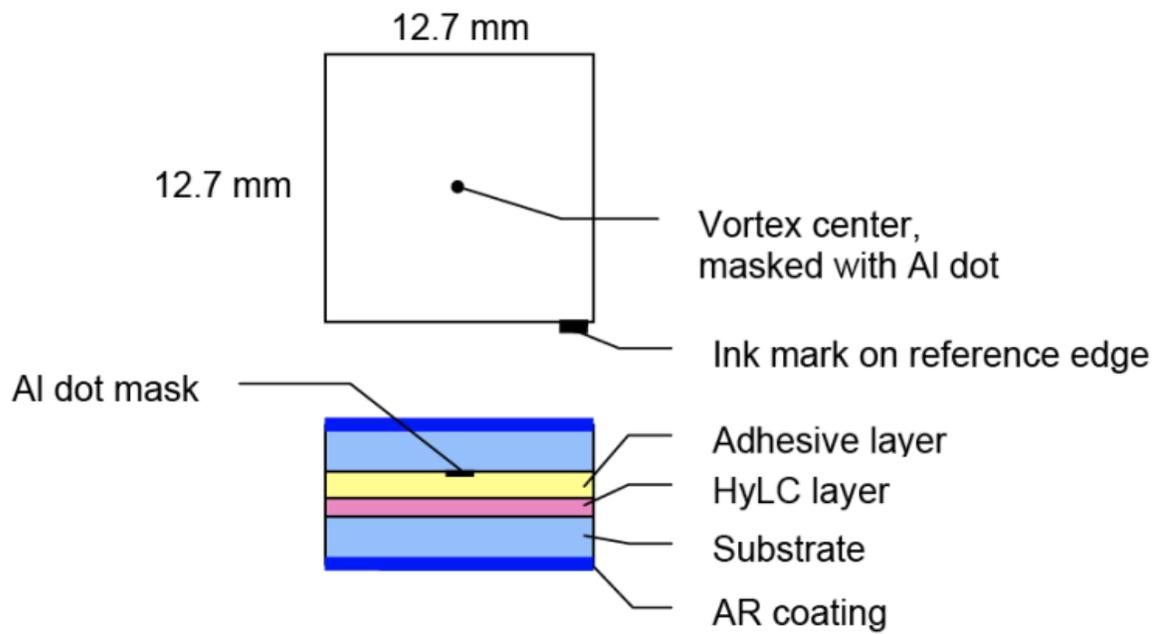
Figure 3. *Cross-section of the sandwich design of the JDSU liquid crystal polymer vortex mask. The hybrid liquid crystal polymer (HyLC) layer is deposited on one substrate and a small opaque dot mask is placed upon another substrate, and the two are then glued together, with the dot centered over the vortex.*

Vortex Mask Specifications

	ATTRIBUTE	PROVISIONAL SPECIFICATION
1.	Substrate Material	N-BALF4
2.	Dimensions	12.5 x 12.5mm
3.	Clear aperture (CA)	10 mm ϕ, centered on the vortex. No polarization defects within CA.
4.	Thickness	1.65 ±0.05 mm
5.	Retarder material	Liquid crystal polymer
6.	Retarder structure	Laminated structure
7.	Angle of incidence	Normal
8.	Illumination cone angle	not specified
9.	Flux density	not specified
10.	Wavelength band (for AR coating)	720~880 nm
11.	HWP center wavelength	λ_0=800 +/- 15 nm
12.	Retardance in clear aperture region	180° at HWP wavelength
13.	Topological charge	n=4
14.	Region of irregularity	≤30 µm; more preferably <20 µm.
15.	Dot mask	An appropriately sized opaque dot mask to be placed over region of irregularity, centered to within 1 micron of the vortex center.
16.	Reference edge	Marked
17.	Transmission	≥97% within the band of interest
18.	Transmitted wavefront irregularity	P-V ≤λ/20 within clear aperture (λ=633)
19.	Scratch/dig	60/40 equivalent within clear aperture
20.	Operating conditions	Room temperature, atm. pressure
21.	Storage conditions	-40 to 70° C; 10 to 90%RH, non-condensing

2.4. HCIT configuration

Even with a perfect vortex mask, extra starlight leakage will result if the diffraction point spread function deviates from a perfect Airy pattern positioned exactly on the center of the vortex (e.g., Mawet et al. 2011a and Serabyn & Mawet 2012b). Extraneous sources of diffracted and scattered light must thus be carefully controlled and/or suppressed, and so much of our experimental efforts were aimed at understanding the limitations of the facility itself, and in modifying the system (Fig. 4) so as to enable measurements in the desired high-contrast regime. Several steps were crucial to reaching contrasts safely below the milestone level of 10^{-9}, but none of the individual steps brought improvements of more than a factor of 2 or so. Thus several small improvements were combined to cross the 10^{-9} threshold securely. The important factors are listed below, in the order that the HCIT optical elements are encountered:

- For these monochromatic single-polarization tests, a fiber-based polarization controller was used to rotate the input fiber's output polarization state to match a downstream free-space vertical polarizer.

- After launching the input beam into free space, a relatively pure circularly-polarized input state was defined by means of a vertically-oriented free space linear polarizer and a quarter wave plate oriented at 45 degrees.

- The spatial mode was next filtered by passage through an approximately 5 μm diameter pinhole (as in earlier HCIT work).

- Initial tests were carried out for three pupil stops (with diameters of 24, 32 and 40 mm) placed on the HCIT's deformable mirror. Best contrasts were obtained for 24 mm, and this stop was used for the three final monochromatic milestone runs. For this stop size, the focal plane F/# was 64.3.

- The pointing and focus of the input beam were carefully matched to the vortex center. Both focal plane and pupil plane pointing algorithms were investigated. In some cases, a very small pointing offset was inserted to allow for subsequent drifts, as no active tip-tilt mirror was available in the optical system.

- A clear circular (10 mm diameter) Lyot stop 83% the diameter of the demagnified (x 0.5) input pupil was used.

- A circular polarizer downstream of the Lyot stop was used to select the desired high contrast polarization state.

- A "reverse-D"-shaped field stop was used in the post-Lyot-stop focal plane to block most of the light exterior to the 3-8 λ/D dark hole. The field stop was only slightly oversized (~ 1 λ/D) relative to the desired dark hole.

The final optical layout of the HCIT Lyot table as used for our milestone demonstrations is shown in Figure 4 (Serabyn et al. 2013, 2014). As usual, the optical system resides in its vacuum chamber, which is evacuated to ~10 milliTorr levels.
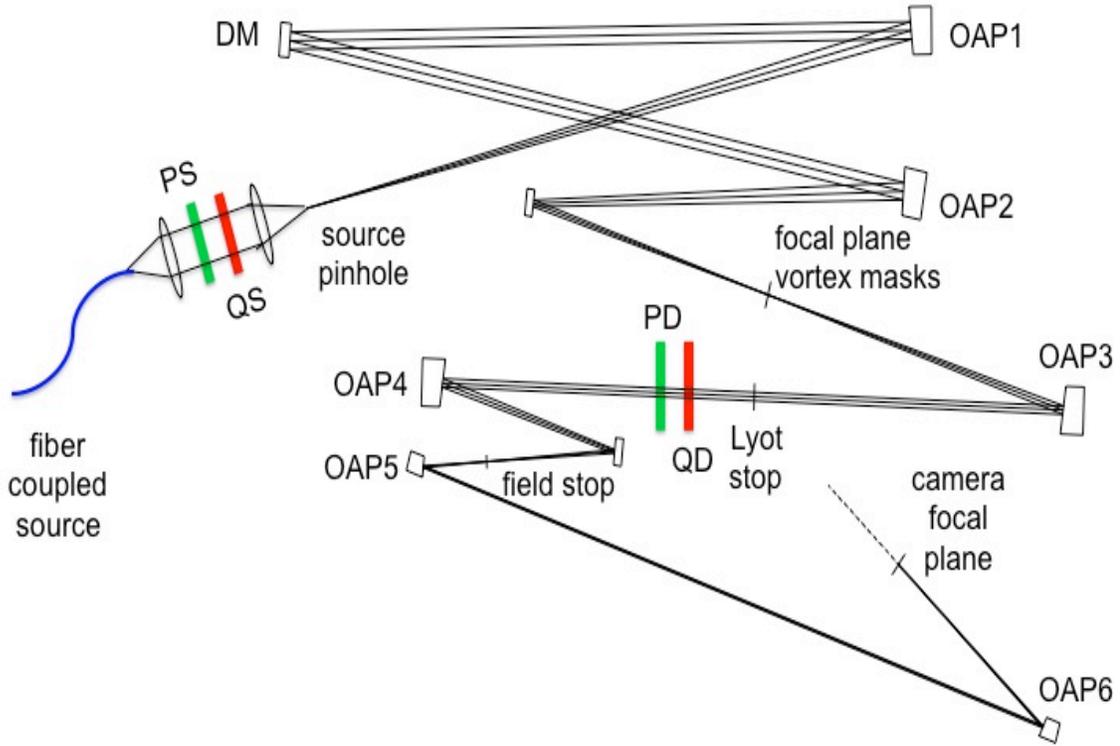
Figure 4. *Schematic of the HCIT optical layout, as used for our 2012/2013 vortex coronagraph tests. The input light is first circularly polarized with the combination of a fiber polarization controller (not shown) and a free-space "source" linear polarizer (PS) and quarter wave plate (QS), after which it is spatially filtered by means of a pinhole approximately 5 μm in diameter. The light is then collimated by the first off-axis paraboloid (OAP), reflects off of the deformable mirror (DM), where the circular aperture stop resides, and is focused onto the vortex phase mask (which resides on a coarse/fine positioning stage). The light is then re-collimated for passage through a clear Lyot stop and a downstream quarter wave plate (QD) and linear polarizer (PD). Finally, the light is focused onto a reverse-D-shaped field stop that is slightly oversized relative to the desired dark hole, and relayed to the camera.*

2.5. Differences Between Flight and Laboratory Demonstrations

There are several important differences between the laboratory demonstration and flight implementation. Each is addressed briefly here.

Starlight: In a space coronagraph, the spectrum of light illuminating the coronagraph would closely resemble black body radiation. For this first milestone, the source was a monochromatic laser. The laser provides a photon flux that is comparable to or somewhat brighter than the target stars to be observed. The goal of this milestone was to demonstrate the contrast that can be achieved, without consideration of the source intensity. A bright source is a convenience that does not compromise the integrity of the demonstration, as it affects only integration times.

Moreover, unlike the light collected by a telescope from a target star, the light intensity is not completely uniform across the pupil. Typically this non-uniformity is a center-to-edge "droop" of a few percent corresponding to the diffraction pattern from the small pinhole. This small level of non-uniformity is expected to have negligible effect on the final contrast, as the wavefront control algorithm accommodates these small effects without the need for improvement in the illumination uniformity.

Spacecraft dynamics: A control system is required in flight to stabilize the light path against motions of the spacecraft. The dominant effects of spacecraft dynamics are jitter of the star image on the coronagraph focal plane mask and beam walk in the optics upstream of the focal plane mask. For a specific example, the ACCESS analysis showed that for fourth-order coronagraphs (including Lyot, vortex, and pupil mapping coronagraphs) with an inner working angle of $3\lambda/D$, pointing errors need to be less than $\pm0.03\ \lambda/D$ rms to limit the corresponding contrast degradation to less than 2×10^{-10}. The concept models have shown that the required pointing stability can be achieved in space with current high Technology Readiness Level (TRL) systems. Scaled to the HCIT, this would correspond to an ability to center the vortex mask on the "star" within 1.5 μm, or about 0.35 pixel when projected to the CCD focal plane.

The milestone demonstration requires the stability of the testbed, including the centration of the star on the vortex as one example, which is untraceable to spacecraft dynamics. In practice, the HCIT often exhibits alignment drifts that are larger than expected in the space environment, but these tend to decrease with time under vacuum. As such we relied on favorable periods of thermal and mechanical stability of the HCIT, and in some cases, included a slight pointing offset to allow drifting toward the optimum pointing.

Single deformable mirror: The milestone demonstrations were carried out with a single DM, which allows the control of phase and amplitude in the complex wavefront over one half of the coronagraph field described. In flight, it is expected that a pair of DMs will be used, in series, to generate a full (two-sided) dark field, with the added advantages of a deeper contrast field and better broadband control.

On the other hand, with the exception of the second DM, and the actual size of the DM, the layout of the vortex coronagraph in the HCIT is essentially the same as is being proposed for space (ACCESS; Trauger et al. 2010). The layout also allows us to investigate the need to separate polarization states to reach high contrast prior to the definition of the flight system.

3. Computation of the Metric

3.1. Definitions

The contrast metric requires a measurement of the intensity of speckles appearing within the dark field, relative to the intensity of the incident star. The contrast metric will be assessed in terms of statistical confidence to capture the impact of experimental noise and uncertainties. In the following paragraphs we define the terms involved in this process, spell out the measurement steps, and specify the data products.

3.1.1. "Raw" Image and "Calibrated" Image. Standard techniques for the acquisition of CCD images are used. We define a "raw" image to be the pixel-by-pixel image obtained by reading the charge from each pixel of the CCD, amplifying and sending it to an analog-to-digital converter. We define a "calibrated" image to be a raw image that has had background bias subtracted and the detector responsivity normalized by dividing by a flat-field image. Saturated images are avoided in order to avoid the confusion of CCD blooming and other potential CCD nonlinearities. All raw images are permanently archived and available for later analysis.

3.1.2. We define "scratch" to be a DM setting in which actuators are set to a predetermined surface figure that is approximately flat (~ 20 volts on each actuator).

3.1.3. We define the "star" to be a small pinhole illuminated with laser light relayed via optical fiber from a source outside the HCIT vacuum wall. The "small" pinhole is unresolved by the optical system; e.g., a 5-μm diameter pinhole is "small" and unresolved by the 51 μm FWHM Airy disk in our F/64.3 beam at 785 nm wavelength. This "star" is the only source of light in the optical path of the HCIT. It is a stand-in for the star image that would have been formed by a telescope system.

3.1.4. We define the "algorithm" to be the computer code that takes as input the measured speckle field images, and produces as output a voltage value to be applied to each element of the DM, with the goal of reducing the intensity of speckles.

3.1.5. The "contrast field" is a dimensionless map representing, for each pixel of the detector, the ratio of its value to the value of the peak of the central PSF that would be measured in the same testbed conditions (light source, exposure time, Lyot stop, etc.) if the coronagraph focal plane mask were removed. The calibration of the contrast field is further detailed in Sections 3.2 and 3.3.

3.1.6. The "contrast value" is a dimensionless quantity that is the average value of the contrast field over the dark field adopted for the experiment.

3.1.7. "Statistical Confidence". The interpretation of measured numerical contrast values shall take into consideration, in an appropriate way, the statistics of measurement, including detector read noise, photon counting noise, and dark noise.

The milestone objective is to demonstrate with high confidence that the true contrast value in the dark field, as estimated from our measurements, is equal to or better than the required threshold contrast value C_0. The estimated true contrast value shall be obtained from the average of the set of four or more contrast values measured in a continuous sequence (over an expected period of approximately one hour).

For this milestone the required threshold is a mean contrast value of $C_0 = 1.0 \times 10^{-9}$ with a confidence of 90% or better. Estimation of this statistical confidence level requires an estimation of variances. Given that our speckle fields contain a mix of static and quasi-static speckles (the residual speckle field remaining after the completion of a wavefront sensing and control cycle, together with the effects of alignment drift following the control cycle), as well as other sources of measurement noise including photon detection statistics and CCD read noise, an analytical development of speckle statistics is impractical. Our approach is to compute the confidence coefficients on the assumption of Gaussian statistics, but also to make the full set of measurements available to enable computation of the confidence levels for other statistics.

At any time in the demonstration, the true contrast is subject to laboratory conditions, including the quality of the optical components, their alignment, any drift in their alignment over time, and the effectiveness of each wavefront sensing and control cycle. With each iteration, our nulling procedure attempts to improve the contrast value, thus compensating for any drift or changes in alignment that may have occurred since the previous iteration, and further variations may be expected due to experimental noise and any limitations in the algorithm. The data set built up from a sequence of such iterations provides a distribution of contrast values, which will be regarded as Gaussian about a mean contrast for the data set. We therefore consider the mean contrast value as representative of the true contrast value for a data set, and the distribution of contrast determinations among the iterations within the data set as a combination of both random wavefront control errors and random measurement errors.

The mean contrast values and confidence limits are computed as follows. The average of one or more images taken at the completion of each iteration is used to compute the contrast value c_i. The mean contrast for a set of images taken in a given sequence is:

$$\hat{c} = \sum_{i=1}^{n} \frac{c_i}{n}$$

where n is the number of images in each set. The standard deviation σ_{each} in the contrast values c_i obtained for individual images within the set, which now includes both the measurement noise and the (assumed random) contrast variations due to changes in the DM settings for each speckle nulling iteration, is:

$$\sigma_{each} = \sqrt{\sum_{i=1}^{n} \frac{(c_i - \hat{c})^2}{n-1}}$$

Our estimate $\hat{c}$ is subject to uncertainty in the contrast measurements $\sigma_{mean} = \sigma_{each}/\sqrt{n}$ and the independently-determined photometry error σ_{phot}. With the approximation that the contrast values have a Gaussian distribution about the mean contrast, the statistical confidence that the mean contrast is less than $C_0 = 1 \times 10^{-9}$ is given by:

$$conf = \frac{1}{\sqrt{2\pi}} \int_{-\infty}^{t} e^{-z^2/2} dz$$

where $t = (C_0 - \hat{c})/\sigma$ and $\sigma = \sqrt{\sigma_{mean}^2 + \sigma_{phot}^2}$. The values $\hat{c}$ and σ are the milestone metrics. The 90% confidence value is the value C_0 such that $conf(C_0) = 0.9$.

3.2. Measurement of the Star Brightness

The brightness of the star during our dark hole exposures was determined by means of two calibration ratios, r_1 and r_2, defined and measured as follows:

First, short-exposure, unsaturated images with the full stellar flux were obtained by offsetting the vortex mask laterally in the focal plane by approximately 1 mm, leaving all coronagraphic elements other than focal-plane vortex mask in place. A number of such short-exposure ($\sim$ 1 msec) images of the star were averaged, to increase the signal to noise ratio. From this final averaged "star image", we calculated the first calibration ratio, defined here as r_1, of the peak stellar pixel, P, to the sum, Σ_{PSF}, of all pixels in the PSF out to ±200 pixels in both x and y. Note that this ratio is independent of the exposure time, as both factors arise in the same image. We obtained r_1 = 0.00401 ± 0.00003.

Second, longer exposure images were used to obtain a second ratio, r_2, defined as the ratio of Σ_{PSF} to Σ_{sp}, where Σ_{sp} is the sum of all flux within an off-center speckle field located outside of the desired dark hole. To obtain r_2, pairs of images with nearly identical optical configurations were used: the first image again being the direct stellar image, as above, while for the second image, the vortex was slid into place. The first of these images again gives Σ_{PSF}, but with a longer integration time, which leads to saturation of the peak of the PSF. Luckily, summation over the PSF is insensitive to saturation (blooming up and down the CCD column) of the peak of the PSF, as long as the blooming does not extend beyond the summation area in the image, because the CCD conserves electrons. All electrons are counted because the blooming occurs at a value (~40,000 DN/pixel) that is well below the digitization limit (64000 DN/pixel), as has been verified (5/12/2013) by testing the linearity of the summed PSF signal for various exposure times. This allowed us to use convenient exposure times to measure both the PSF sum (~0.016 sec) and off-center speckle sum (10 sec) with adequate S/N in a small number of exposures.

The reason for the above procedure is that the same off-axis speckle field is directly accessible in dark field images (in which the field stop has been removed; field stop removal was thus part of our measurement cycle). In particular, the ratio $r_1r_2 = P/\Sigma_{sp}$ thus allows us to scale directly from the measured Σ_{sp} in our dark field images to P, the brightest pixel in the stellar image at the time of the dark field measurement. We measured r_1r_2 on three separate occasions, and obtained r_1r_2 = 238.4, with an rms deviation of 4%. Thus σ_{phot} is 4%, in relative units.

## 3.3. Measurement of the Coronagraph Contrast Field

Each "coronagraph contrast field" is obtained as follows:

3.3.1. The vortex mask is centered on the star image.

3.3.2. An image (typical exposure times for the milestone runs were 2 min) is taken of the coronagraph field (the suppressed star and surrounding speckle field). The dimensions of the target areas, as shown schematically in Figure 5, are defined as follows: A dark (D-shaped) field extending from 3 to 8 λ/D, representing a useful inner

15

search space, is bounded by a straight line that passes $3\,\lambda/D$ from the star at its closest point, and by a circle of radius $8\,\lambda/D$ centered on the star.

3.3.3. Each image is normalized to the "star brightness" as defined and described in 3.2, i.e., the fixed relationship between peak star brightness and the integrated light in the speckle field outside the central DM-controlled area was used to estimate the star brightness associated with each coronagraph image.
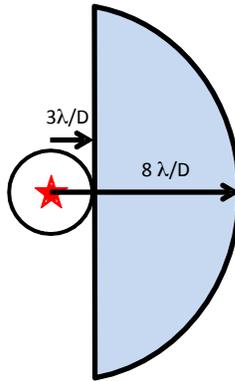
Figure 5. *Target high-contrast dark field. As described in the text, inner and outer regions are defined for the one-sided dark field. The location of the suppressed central star is indicated in red. The target dark hole for this initial demonstration is from 3 to 8 λ/D, as defined in this figure.*

3.3.4. The contrast field image is averaged over the target high-contrast areas, to produce the contrast value. To be explicit, the contrast value is the sum of all contrast values, computed pixel-by-pixel in the dark field area, divided by the total number of pixels in the dark field area, without any weighting being applied. The rms in a given area can also be calculated from the contrast field image.

3.4. Milestone Demonstration Procedure

The procedure for the milestone demonstration is as follows:

3.4.1. The DM is set to scratch. An initial coronagraph contrast field image is obtained as described in Sec. 3.3.

3.4.2. Wavefront sensing and control is performed to find settings of the DM actuators that give the required high-contrast in the target dark field. This iterative procedure may take from one to several hours, starting from scratch, if no prior information is available. It can also take more or less time depending on the stability of the HCIT optical system.

3.4.3. A number of contrast field images are taken, following steps 3.3.1 – 3.3.2. The result at this point is a set of contrast field images. It is required that a sufficient number of images are taken to provide statistical confidence that the milestone contrast levels have been achieved, as described in Section 3.1.7 above.

3.4.4. Laboratory data are archived for future reference, including raw and calibrated images of the reference star and contrast field images.

4. Success Criteria

The following are the required elements of the milestone demonstration. Each element includes a brief rationale.

4.1. Illumination is monochromatic (or a few percent bandwidth) light in single or dual polarization at a wavelength in the range of 400 nm $< \lambda < 900$ nm.

Rationale: *This milestone is an initial demonstration of the feasibility of the approach at a wavelength in the science band of TPF-C or Exo-C.*

4.2. A mean contrast metric of 1 x 10^{-9} or smaller shall be achieved in a 3 to 8 λ/D dark zone, as defined in Sec. 3.3.2.

Rationale: *This provides evidence that the high contrast field is sufficiently dark (10^{-9} expected exozodi level) to be useful for searching planets, and to carry out initial tests at small angles.*

4.3. Criterion 4.2, averaged over the data set, shall be met with a confidence of 90% or better, as defined in Sec. 3.1.5. Sufficient data must be taken to justify this statistical confidence.

Rationale: *Assuming the contrast values have a Gaussian distribution about the mean contrast, this demonstrates a statistical confidence of 90% that the mean contrast goal has been reached.*

4.4. Elements 4.1 – 4.3 must be satisfied on three separate occasions with a reset of the wavefront control system software (DM set to scratch) between each demonstration.

Rationale: *This provides evidence of the repeatability of the contrast demonstration.*

The wavefront control system software reset between data sets ensures that the three data sets can be considered as independent and do not represent an unusually good configuration that cannot be reproduced. For each demonstration the DM will begin from a "scratch" setting. There is no time requirement for the demonstrations, other than the time required to meet the statistics stipulated in the success criteria. There is no required interval between demonstrations; subsequent demonstrations can begin as soon as prior demonstrations have ended. There is also no requirement to turn off power, open the vacuum tank, or delete data relevant for the calibration of the DM influence function.

5. Certification

The PI will assemble a milestone certification data package for review by the ExEPTAC and the ExEP program. In the event of a consensus determination that the success criteria have been met, the project will submit the findings of the review board, together with the certification data package, to NASA HQ for official certification of milestone compliance. In the event of a disagreement between the ExEP project and the ExEPTAC, NASA HQ will determine whether to accept the data package and certify compliance or request additional work.

5.1. Milestone Certification Data Package

The milestone certification data package will contain the following explanations, charts, and data products.

5.1.1. A narrative report, including a discussion of how each element of the milestone was met, and a narrative summary of the overall milestone achievement.

5.1.2. A description of the optical elements, including the vortex masks, and their significant characteristics.

5.1.3. A tabulation of the significant operating parameters of the apparatus.

5.1.4. A calibrated image of the reference star, and the photometry method used.

5.1.5. A calibrated image of the (distant) off-axis transmission of the vortex mask.

5.1.6. A contrast field image representative of the data set, with appropriate numerical contrast values indicated, with coordinate scales indicated in units of Airy distance (λ/D).

5.1.7. For each image reported as part of the milestone demonstration, the average contrast recorded within the area spanning 3-4 λ/D.

5.1.8. A description of the data reduction algorithms, in sufficient detail to guide an independent analysis of the delivered data.

5.1.9. Contrast metric values and supporting statistics for the overall data used to satisfy the milestone requirements, including a pixel-by-pixel histogram of contrast values across the dark field.

6. Demonstration Results

Contrast tests in monochromatic light were carried out in the HCIT with a laser diode source at a wavelength, λ, of 785 nm. The milestone demonstrations relied on a wavefront sensing and correction process that has been used in previous high-contrast demonstrations: the "electric field conjugation" (EFC) method (Give'on *et al*. (2007), that was applied as follows. For a given wavelength, and starting with a nominally flat surface figure setting on the DM for each run, we: (a) take a set of contrast field images with the initial DM setting; (b) take images for each of four "probe" DM settings (consisting of small deterministic surface figure deviations from the initial DM setting), (c) use these data to compute the complex electric field in the target dark field region; and then (d) calculate and apply a new DM setting that will reduce the energy over the dark field, thus establishing a new "initial DM setting" in preparation for the next iteration, which is a loop back to step (a). For the milestone runs, because of low photon levels in the ultimate dark hole, integration times for individual dark hole images were 120 sec, and one complete wavefront sensing and control cycle, including overhead for CCD readouts, data handling and computations, thus took about 10 minutes.

Figure 7 shows the contrast improvement as a function of iteration cycle (i.e., time) for our first milestone run. The contrast plotted is the ratio of dark hole level to the starlight level, as described earlier. As Fig. 7 shows, the initial improvement to roughly the 10^{-9} level is quite fast, taking only a handful of iterations, after which the contrast improves

more slowly for the last factor of ~ 2. This change in slope occurs roughly where the read noise becomes important. Even this final improvement could have been sped up, but celerity was not a goal in these laboratory demonstrations, while stability was, as was specifically specified by the whitepaper. Thus, slower convergence parameters were selected for better stability of the system below the 10^{-9} level. As Fig. 7 demonstrates, many hours were successfully spent at average contrasts below 10^{-9}, with contrasts that continued to slowly improve.
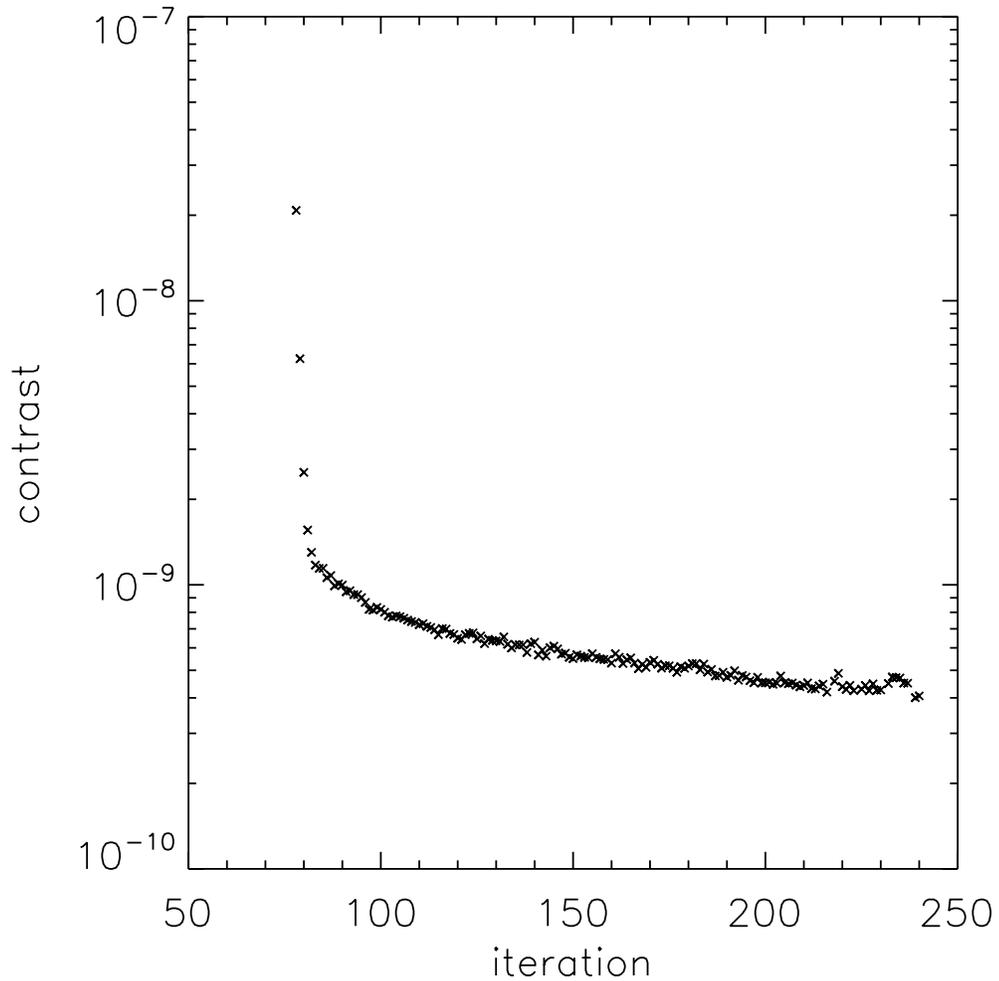
Figure 7. *Contrast improvement in the 3-8 λ/D region during our first milestone run.*

The three dark holes reached at the conclusion of our three milestone runs are shown in Fig. 8a. These three nulling runs each began (on subsequent days) by re-flattening the DM. Each run thus represents an independent wavefront control solution for the dark hole. A schematic of the size and location of the targeted 3-8 λ/D dark hole region relative to the center of the point spread function is shown near the right-hand edge of Fig. 8a. The bottom right hand image of Fig. 8a also shows the size and location of the 3-8 λ/D dark hole on the same image scale as

the three final dark hole images. The outer edge of the bright "reverse-D"-shaped region seen in the images corresponds to the field stop edge, while the wavefront-controlled dark hole is the dim region inside the bright reverse-D. Further detail is provided in Serabyn et al. (2013) and (2014). We note however that 1 λ/D corresponds to 11.6 pixels, so the images are very much over-sampled.
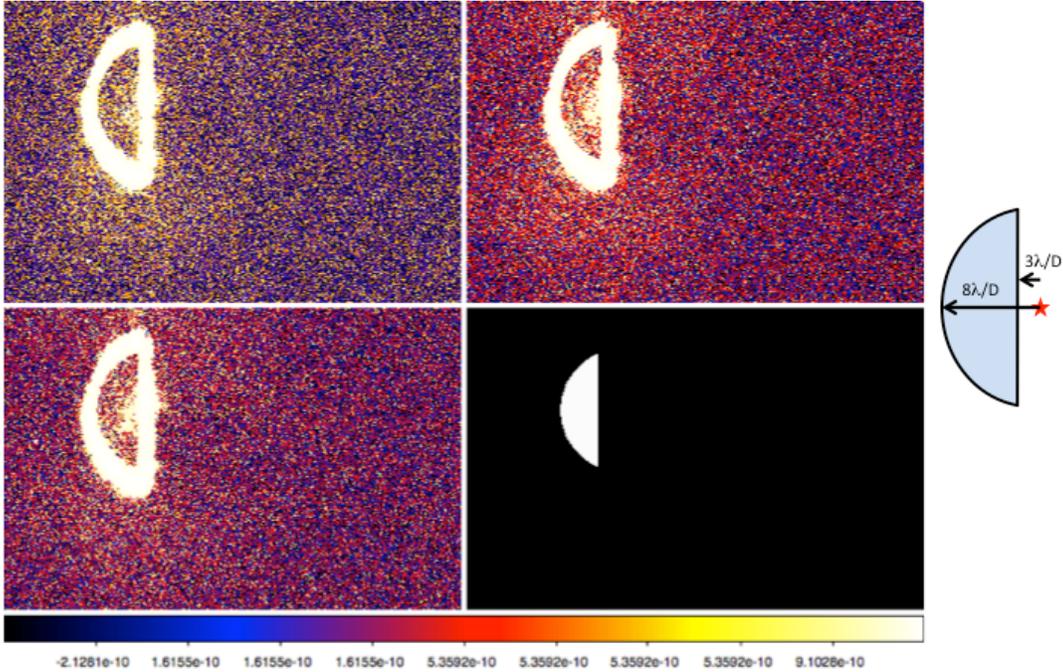
Figure 8a. *Right-hand edge: Schematic of the size and location of the targeted 3-8 λ/D dark hole relative to the location of the point source (red star) in the image plane. Colored panels: three images showing the final dark holes obtained at the end of the three independent milestone nulling runs. Bottom right: the size and location of the 3-8 λ/D dark hole on the same spatial scale.*
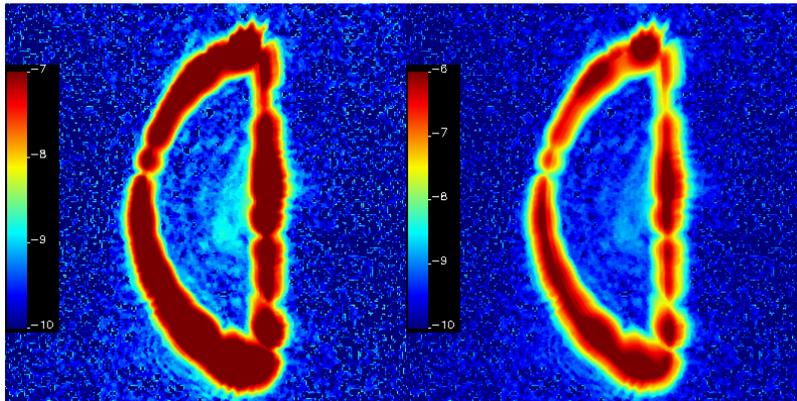

Figure 8b. *The (slightly-smoothed) bottoms of the final dark hole in our second milestone run at two different scaling levels. Note that the 10^{-9} level is aqua-colored in the left hand image, and somewhat darker on the right.*
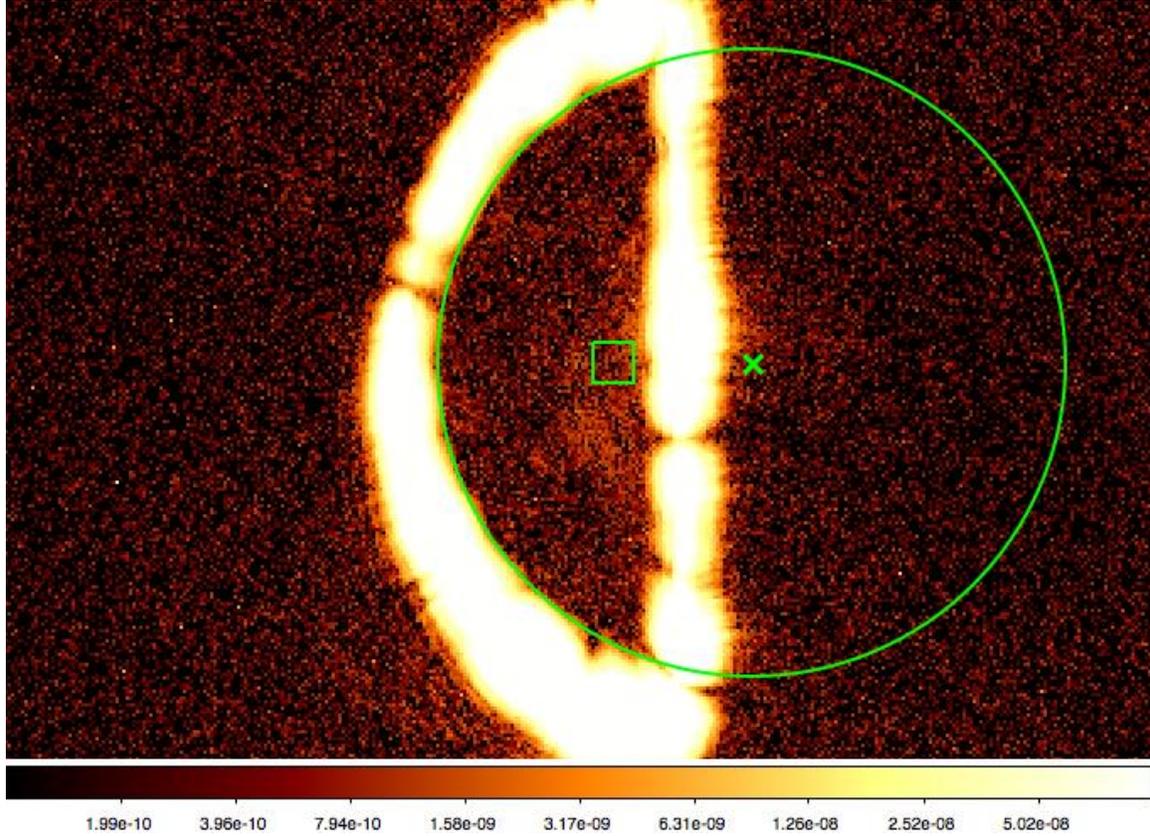
Figure 8c. An overlay of an 8 λ/D circle, a 3-4 λ/D square, and a cross marking the star location on the final dark hole image in our first milestone run.

The observed dark holes can be viewed as "flat" valley floors surrounded by much brighter light leakages along their boundaries. However, these valley floors are in general not entirely flat, as they tend to show increasing brightness toward the stellar position. Moreover, hints of ripply, Airy-pattern-like residues are also present in some cases. Finally, in all cases, the dark hole levels are clearly only somewhat greater than the read noise. Figs. 8b through 8f illustrate these aspects. Fig. 8b shows the bottom of the final dark hole in our second milestone run at two different scaling levels. Fig. 8c shows an overlay of an 8 λ/D circle and a 3-4 λ/D square on the final dark hole image in our first milestone run. Fig. 8d shows the bottoms of the first two milestone runs free of the surrounding glare. Fig. 8e shows radial contrast curves for these same two dark holes, averaged to 1 λ/D bins. Finally, Fig. 8f shows a horizontal cross-cut for the final image in our second milestone run at the pixel scale.
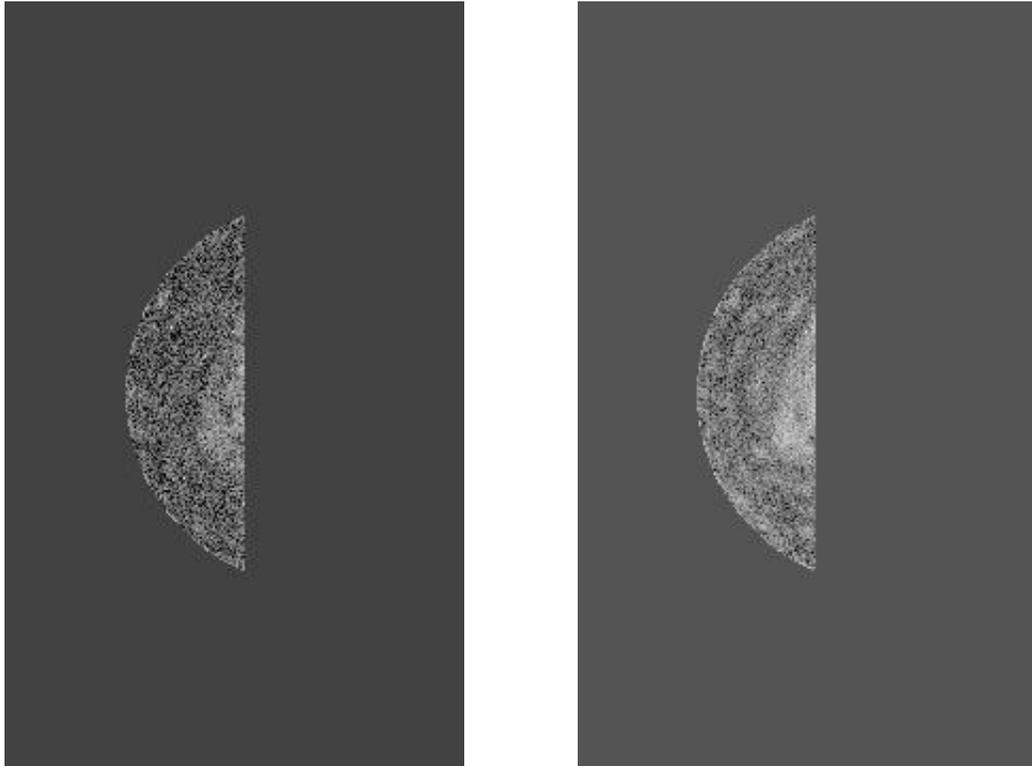
Figure 8d. The bottoms of final dark holes of our first and second milestone runs, without the surrounding glare.
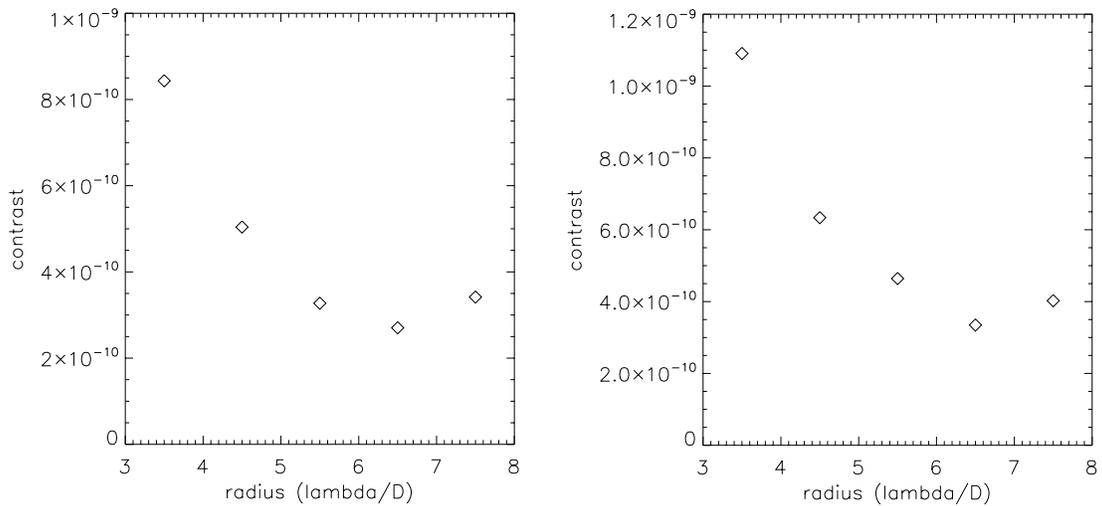
Figure 8e. Radial contrast curves for the same two dark holes of Fig. 8d, averaged to 1 λ/D bins.
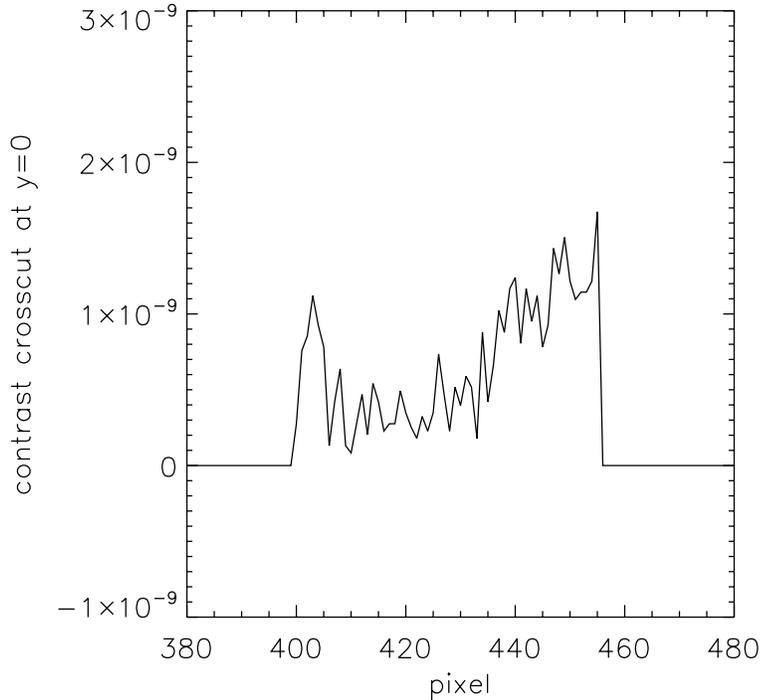
**Figure 8f.** A horizontal cross-cut of the final dark hole in our second milestone run.

Table 2 gives the detailed numerical results of the three milestone runs, with one column for each milestone run. The individual rows give the run dates, the 3-8 λ/D spatial-average dark-hole contrasts (the five c_i's) for the 5 final dark hole images of each milestone run, the temporal averages $(\hat{c})$ of these five 3-8 λ/D spatial-average dark-hole contrasts, σ_{mean}, σ_{phot}, σ, and t for each run, and the temporal average of the 3-4 λ/D average contrasts for these same 5 final iterations in each run (with all quantities as defined in Sect. 3.1.7). Note that the five c_i's listed for the first milestone run correspond to the last five points in Fig. 7. As can be seen in the table, each of the three nulling runs reached similar average dark-hole suppression levels for the 3-8 λ/D region, specifically, $\hat{c}$ = 4.4 x 10^{-10}, 5.3 x 10^{-10}, and 5.2 x 10^{-10}, respectively, with an overall average of 5.0 x 10^{-10}. The final (temporal) σ was uniformly $\approx$ 0.22 x 10^{-10}, implying that our average contrasts are stable at more than 20 σ below the milestone level (i.e., t > 20 in all three cases), so the statistical confidence is indistinguishable from unity. Finally, as also seen in Table 2, the average suppression levels in the innermost 3-4 λ/D region were also quite good, with an average of 1.0 x 10^{-9} for the three milestone runs.

Finally, Figure 9 provides a pixel-by-pixel histogram of contrast values in the dark field obtained at the end of our 2013 May 10 nulling milestone run. Negative values result from the subtraction of the d.c. bias term, which is accompanied by the subtraction of the associated read noise.

Table 2:

Results summary for the 5 final dark hole images in each of the three milestone runs

(using the nomenclature defined in Section 3.1.7)

Milestone Run/Date:	(1) 2013 May 10	(2) 2013 May 13	(3) 2013 May 14
c_1: 3-8 λ/D avg. contrast	4.7×10^{-10}	5.0×10^{-10}	5.2×10^{-10}
c_2: 3-8 λ/D avg. contrast	4.5×10^{-10}	5.2×10^{-10}	5.2×10^{-10}
c_3: 3-8 λ/D avg. contrast	4.5×10^{-10}	5.2×10^{-10}	5.1×10^{-10}
c_4: 3-8 λ/D avg. contrast	4.0×10^{-10}	5.6×10^{-10}	5.4×10^{-10}
c_5: 3-8 λ/D avg. contrast	4.1×10^{-10}	5.4×10^{-10}	5.2×10^{-10}
$\hat{c}$: avg. 3-8 λ/D contrast	**4.4×10^{-10}**	**5.3×10^{-10}**	**5.2×10^{-10}**
σ_{mean}(3-8 λ/D contrast)	0.13×10^{-10}	0.10×10^{-10}	0.05×10^{-10}
σ_{phot} (3-8 λ/D contrast)	0.17×10^{-10}	0.21×10^{-10}	0.21×10^{-10}
σ (3-8 λ/D contrast)	**0.21×10^{-10}**	**0.23×10^{-10}**	**0.22×10^{-10}**
t	26.7	20.4	21.8
avg. 3-4 λ/D contrast	8.6×10^{-10}	1.1×10^{-9}	1.1×10^{-9}
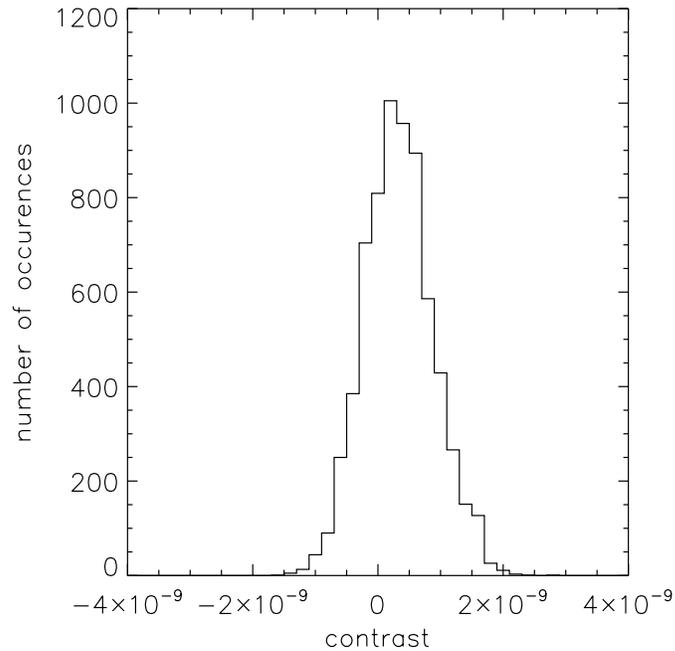
Figure 9. *Histogram of all contrast values within the final dark hole of 2013 May 10.*

7. Summary

The targeted 10^{-9} average monochromatic contrast level within the desired dark field region has been achieved on three independent occasions to a very high level of confidence ($> 20\ \sigma$). The prescribed vortex milestone level has thus been exceeded.

8. References

Give'on, A., Kern, B., Shaklan, S., Moody, D., Pueyo, L., "Broadband wavefront correction algorithm for high-contrast imaging systems," *Proc. SPIE* **6691**, 66910A, 2007.

Guyon, O., Pluzhnik, E.A., Kuchner, M.J., Collins, B., and Ridgway, S.T., "Theoretical Limits On Extrasolar Terrestrial Planet Detection with Coronagraphs," *Ap.J. Suppl.* **167,** 81, 2006.

Levine, M., Shaklan, S. & Kasting, J., "Terrestrial Planet Finder Coronagraph: Science and Technology Definition Team Report," JPL Publ. D-34923, 2006.

Mawet, D., Riaud, P., Absil, O. & Surdej, J., "Annular Groove Phase Mask Coronagraph," *ApJ*, **633**, 1191, 2005.

Mawet, D. Serabyn, E.,Liewer,K., Hanot, Ch., McEldowney, S., Shemo, D. & O'Brien, N., "Optical Vectorial Vortex Coronagraphs using Liquid Crystal Polymers: Theory, Manufacturing and Laboratory Demonstration," *Optics Express,* **17**, 1902, 2009.

Mawet, D. *et al.*, "Taking the vector vortex coronagraph to the next level for ground- and space-based exoplanet imaging instruments: review of technology developments in the USA, Japan, and Europe," *Proc. SPIE* **8151**, 815108-1, 2011a.

Mawet, D., *et al.*, "Recent Results of the Second Generation of Vector Vortex Coronagraphs on the High-contrast Imaging Testbed at JPL," *Proc. SPIE* **8151**, 81511D-8, 2011b.

Serabyn E., D. Mawet & R. Burruss, "The potential of small space telescopes for exoplanet observations," *Proc. SPIE* **7731**, 77312O, 2010.

Serabyn, E. & Mawet, D., "Detecting Exoplanets with a Liquid-Crystal-Based Vortex Coronagraph," *Mol. Cryst. Liq. Cryst.* **559**, 69, 2012a.

Serabyn E., & Mawet, D., "Technology Development for Space Based Vortex Coronagraphy," Proc. **2012 IEEE Aerospace Conf.**, DOI: 10.1109/AERO.2012.6187180, 2012b.

Serabyn, E., Trauger, J., Moody, D., Mawet, D., Liewer, K., Krist, J., Kern, B., "High-contrast imaging results with the vortex coronagraph," *Proc. SPIE* **8864**, 88640Y-1, 2013.

Serabyn, E., Cady, E., Kern, B. and Mawet, D., "High Contrast Demonstrations with the Vortex Coronagraph," Proc. **2014 IEEE Aerosp. Conf.,** in press.

Swartzlander, G., "The optical vortex coronagraph, " *J. Opt. A.*, **11**, 1464, 2009.

Trauger, J. *et al.,* "TPF-C Milestone #1 Report," JPL Document D-35484, 2006.

Trauger, J. and W. Traub, "A laboratory demonstration of the capability to image an Earth-like extrasolar planet," *Nature* **446**, 771, 2007.

Trauger, J. *et al.*, "Laboratory demonstrations of high-contrast imaging for space coronagraphy," *Proc. SPIE* **6693**, 66930X, 2007.

Trauger, J. *et al.*, "ACCESS – A Concept Study for the Direct Imaging and Spectroscopy of Exoplanetary Systems," in "Pathways towards Habitable Planets," *ASP Conf. Series* **430***, 375, 2010.